Earth, Planets and Space

FULL PAPER Open Access

Local time and longitudinal variation of the ionospheric radial current: swarm observations and TIE–GCM simulations

Hui Wang, Hao Xia, Kedeng Zhang*, Yunfang Zhong and Chenyu Qian

Abstract

Based on the high-precision vector magnetic field data of Swarm A and C satellites, we perform a statistical analysis of the diurnal and longitudinal variations of the ionospheric radial current (IRC) in the F layer at the magnetic equator from 2014 to 2018. The observations are compared with the simulations based on the Thermosphere–Ionosphere Electrodynamics–General Circulation Model (TIE–GCM). It is found that the noon IRC is radially outward, whereas the dusk IRC is radially inward. The time of the change from the inward to the outward direction occurred is earlier in June than in other seasons. The TIE–GCM results show that low atmospheric tides have an important effect on the seasonal change in the reverse time. The noon IRC is weakened primarily by the polarization current from migrating tides. The dusk IRC is mainly weakened by polarization current from nonmigrating tides in the equinox and December solstice and by dynamo current from migrating tides in the June solstice. Geomagnetic field configuration is the main reason for the longitudinal variation of IRC. The noon IRC have a wave-4 zonal structure, which is mainly caused by the outward propagation of migrating and nonmigrating tides. The dusk IRC in the western hemisphere shows a larger current density than that in the eastern hemisphere, resulting mainly from the neutral wind dynamo current. The competing effect of the wind dynamo current and polarization current determined the peak location of the total current in the western hemisphere.

Keywords: Ionosphere radical current, F region dynamo, Low atmospheric tides, Swarm satellites, Thermosphere–ionosphere electrodynamics general circulation model

*Correspondence: ninghe_zkd@whu.edu.cn

Department of Space Physics, School of Electronic Information, Wuhan University, Wuhan 430070, China

Graphical Abstract

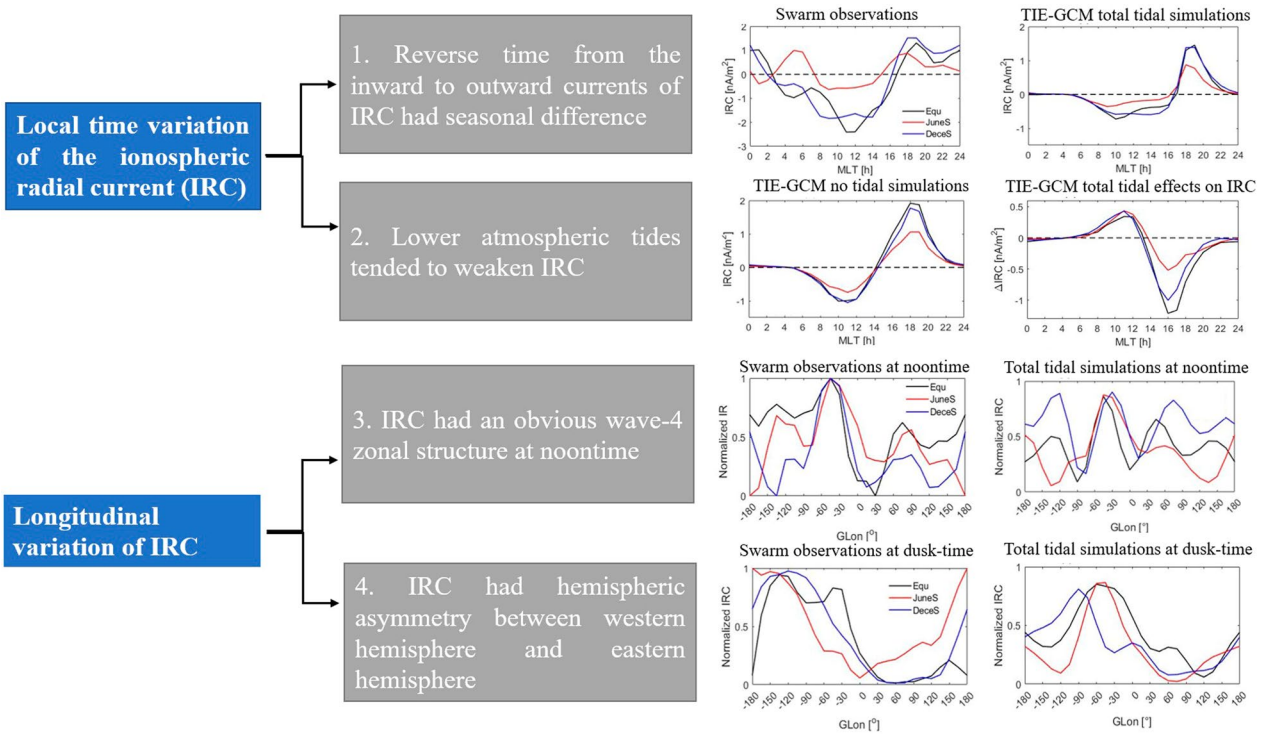

Introduction

Ionospheric currents play an important role in the electrodynamic coupling in the geospace. During periods of disturbance, they are the main factors that cause geomagnetically induced currents, which may damage electrical power grids and degrade radio communication and navigation systems. The eastward and westward zonal winds in the F region of the thermosphere above the magnetic equator drive the radially outward and inward ionospheric radial currents (IRCs), respectively. IRCs are diverted into the field-aligned currents (FACs) in the northern and southern hemispheres, which are closed by horizontal currents in the E layer (Rishbeth 1971a, b). Maeda et al. (1982) compared the Magsat magnetic field data with the ground-based magnetic field data for November and December 1979. They revealed a significant change in the D component of the geomagnetic field in the dusk at the magnetic equator. As an explanation, they proposed the presence of a FAC and a radially outward current system.

Because the thermospheric zonal wind has different directions during the daytime and night-time, there is a significant local time variation in the distribution of the IRC. Olsen et al. (1997) decomposed the magnetic field from the Magsat data into two parts, toroidal and poloidal. They found a radially inward current around noon and an outward current around dusk above the dip equator. Lühr and Maus (2006) used magnetic field data from CHAllenging Minisatellite Payload (CHAMP) to calculate the IRC around noon and dusk. One of their findings was that IRC around noon is stronger than that around dusk. The noon inward IRC driven by the westward neutral wind reaches 6 mA/m, whereas the dusk outward IRC driven by the eastward wind reaches 4 mA/m. Park et al. (2010) used CHAMP magnetic field data from 2001 to 2004 to study the diurnal variation in the IRC. They found that IRC has the highest current density around noon and dusk. The current changes direction at 15 magnetic local time (MLT), which is caused by the zonal wind changing from westward to eastward. In addition, Park et al. (2010) found that IRC is weaker in the June solstice (JS), and the difference in current intensity between noon and dusk in JS was not significant. Lühr et al. (2015) used observations from Swarm A and C dual satellites from April to November 2014 and found that above the magnetic equator, IRC is inward at noon and outward at 18 MLT.

Maeda et al. (1982) were the first to relate the change in IRC to geographic longitude (GLon). They found that the magnitude of the D component of the magnetic field observed by Magsat is larger in South America and weaker in India. They speculated that this is related to the longitudinal differences in IRC. Park et al. (2010) used CHAMP observation data and found that the noon IRC at the equinox and JS shows a wave-4 longitudinal structure. However, the wave-4 longitudinal structure is not evident at the dusk, which is related to the reduced coupling efficiency between the E and F layers in the dusk. Lühr et al. (2015) found that the noon IRC is stronger at 0–210° E GLon, whereas the dusk IRC is stronger at 150–300° E GLon. Lühr et al. (2019) performed a detailed analysis of the longitudinal variation in IRC. They found that the noon IRC in the western hemisphere is weaker than that in the eastern hemisphere, whereas the dusk IRC in the western hemisphere is stronger than that in the eastern hemisphere. They speculated that this is because the noon dynamo center is higher in the eastern hemisphere than in the western hemisphere, whereas the dusk dynamo is higher in the western hemisphere. Moreover, they found that the enhanced dusk-time IRC in the South Atlantic Anomaly is related to a weaker geomagnetic field.

These studies have provided much interesting information for understanding IRC; however, the physical mechanism of the MLT and longitudinal distributions of IRC remained unclear. In this work, by analyzing IRC observations from dual Swarm A and C satellites and applying the thermosphere–ionosphere electrodynamics–general circulation model (TIE–GCM), we address in depth the mechanism generating diurnal and longitudinal variations of the IRC. The simulation results were compared with actual observations for the first validation of the model performance.

"Satellite and model" Section briefly introduces the methods used for the data processing and model simulation. "Statistical results" Section compares the statistical results with the model outputs. "Discussion" Section discusses the results in the context of previous studies. Finally, "Conclusions" Section presents the conclusions.

Satellite and model

Swarm satellites

The Swarm satellite constellation was launched by the European Space Agency on November 22, 2013. Swarm satellites A and C fly at altitudes of approximately 470 km, with a longitudinal separation of 1.4°. Swarm B flies at an altitude 1% higher than Swarm A. In our work, the level-2 product FAC_TMS_2F from ESA has been used. The estimation of IRC from dual-satellite observations is briefly introduced in the present work. For further details, please refer to Lühr et al. (2020) and Ritter et al. (2013). The Earth's core, mantle, lithospheric and disturbance fields of the large-scale magnetopause and ring current are removed from the observed magnetic field using the CHAOS-6 model (Finlay et al. 2016). According to Ampere's circuit law, IRC can be calculated as $j = \frac{1}{\mu_0 A} \oint Bdl$, where μ_0 is the vacuum permeability, B is the disturbance field, and the closed quadrilateral is formed by four observation points of Swarm satellites A and C. It took Swarm satellites 131 days to cover all 24 h of local time. During 2014–2018, the number of events in each local time and seasonal bin were almost evenly distributed. Thus, the seasonal and local time biases of IRC events can be avoided. For statistical analyses, IRC density is binned as a function of magnetic coordinates, local time (LT), and seasons. MLat and MLT were derived from the quasi-dipole latitude, as defined by Richmond (1995).

TIE–GCM model

The TIE–GCM is a three-dimensional time-dependent model of the coupled ionosphere–thermosphere system. It was developed at the High Altitude Observatory of the National Center for Atmospheric Research (NCAR/HAO). The drivers of the TIE–GCM include the high-latitude electric field from the Heelis models (Heelis et al. 1982), solar extreme ultraviolet and ultraviolet spectral fluxes parameterized by the F10.7 index (Richards et al. 1994), and lower atmospheric migrating and nonmigrating diurnal and semi-diurnal tides generated from the Global Scale Wave Model (Hagan and Forbes, 2002). The horizontal resolution was 2.5° geographic latitude × 2.5° Glon. TIE–GCM has a total of 57 pressure levels in the vertical direction, with lower and upper boundaries of 97 km and 700 km, respectively, which are dependent on solar activity. The input parameters of TIE–GCM during the magnetic quiet period were as follows: hemispheric power of 18 GW, cross polar cap potential of 30 kV. The mean $F_{10.7}$ index of 100 sfu was used in the model, which corresponds to the low level solar activity during 2014–2018. For each season, the following cases were examined: with or without migrating and nonmigrating tidal forcing, when considering the IGRF geomagnetic field configuration, or a centered dipole magnetic field, where the geomagnetic axis coincided with the rotation axis. By comparing these cases, the effects of tides and geomagnetic field geometry on the LT and longitudinal variation of the IRC were evaluated.

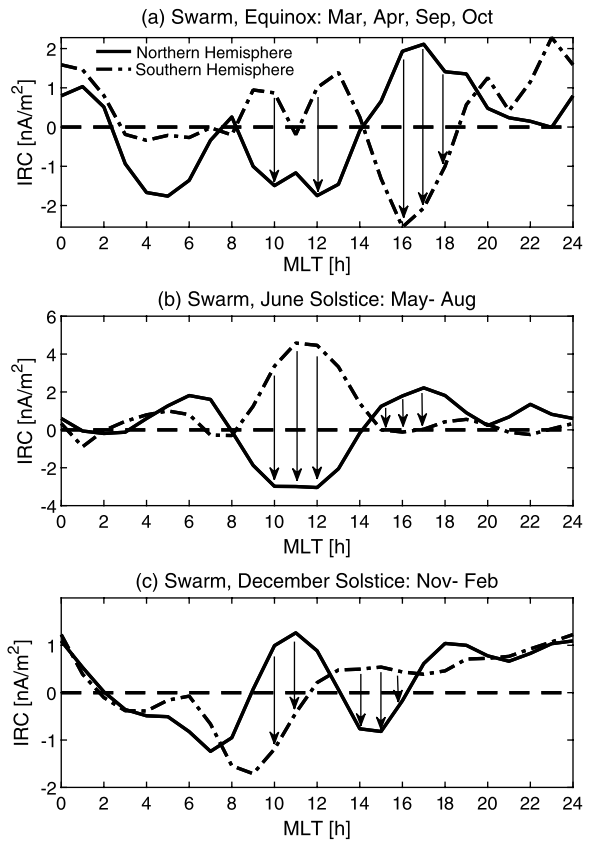

Fig. 1 Local time distributions of the ionospheric radial current (IRC) in the equinox (top), June solstice (JS, middle), and December solstice (DS, bottom). The solid and dashed lines illustrate IRC in the Northern (5°–15° MLat) and Southern Hemispheres (−15° to −5° MLat), respectively. The arrows represent the direction of flow between the northern and southern hemispheres of IRC. The negative and positive values represent the radially inward and outward currents, respectively. The bin width is 1 h in local time. March, April, September, and October were selected for the combined equinox, November to February for DS, and May to August for JS

Statistical results

Diurnal variation

Figure 1 shows the variation in the average radial current at MLT around the 5–15° and −15 to −5° MLat sectors in the equinox, June solstice (JS), and December solstice (DS) from 2014 to 2018. At around 5–15° and − 15 to − 5° MLat, at noontime (10–12 MLT), a large-scale IRC in the equinox is outward in the southern hemisphere and inward in the northern hemisphere. The JS IRC is similar to that in the equinox, but its intensity is, on average, higher. The DS IRC is outward in the northern hemisphere and inward to outward in the southern hemisphere. In this magnetic latitude range, the dusk-time (16–18 MLT) IRC in the equinox is slightly inward to outward in the southern hemisphere and outward in the northern hemisphere. The JS IRC is similar to that in the equinox, but its intensity is weaker. The direction of the DS IRC is from inward to outward in the northern hemisphere and outward in the southern hemisphere.

Previous studies have shown that at low latitudes, interhemispheric field-aligned currents (IHFACs) caused by the hemispheric difference in the solar quiet current systems flow from the winter hemisphere to the summer hemisphere at noontime and dusk-time, and from summer hemisphere to winter hemisphere at dawn, according to Fukushima (1979). However, Park et al. (2011) found that the flow direction is from the summer hemisphere to the winter hemisphere on the dusk side in the equinox and JS. This structure is more complex in DS (Lühr et al. 2019). Therefore, in the equinox and JS, the radial component of the noon-time IHFAC at low latitudes is outward in the southern hemisphere and inward in the northern hemisphere, consistent with the Fukushima's diagram. The radial component of the dusk-time IHFAC is opposite to that at noon, from summer hemisphere to winter hemisphere, which seems to support the results of Park et al. (2011). The December IRC looks more complicated, and the dominant polarity is hard to define. Lühr et al. (2019) found that the direction of IRC at 5–15° MLat is obvious opposite to that at −15 to −5° MLat, which were caused by IHFAC. Hence, the IRC in the region of −15 to −5° and 5–15° MLat is dominated by the radial component of the IHFAC, which is out of the main focus of the present study.

Figure 2 shows the MLT variations of observed and modeled IRC. The simulated IRC have been derived using the equation $j_z = \sigma_P(u_y B_x - E_z)$, where σ_p is the Pedersen conductivity, E_Z is the polarization electric field (positive denotes the outward direction), u_y is the zonal wind (positive means eastward direction), B_x is the geomagnetic field (positive denotes the northward direction) (Park and Lühr, 2012). In this work, the Swarm observed IRC over ± 1° MLat is processed to avoid the influences from IHFAC. Since the latitudinal resolution of TIE–GCM is 2.5° GLat, to ensure enough data in each bin, the modeled IRC over ± 5° MLat is selected. As shown in Fig. 2a, IRC in equinox is radially inward at 02–16 MLT, reaching a peak density of −2.41 nA/m^2 at 11 MLT. In the remaining MLT, IRC is mainly outward, with a peak density of 1.31 nA/m^2 at 19 MLT. JS and DS show similar diurnal variation patterns, but have different peak densities at different local times. In JS (DS), the inward/outward IRC has a peak density of −0.62/0.87 (−1.83/1.52) nA/m^2. Note here that the negative/positive value stands for inward/outward current. In the three seasons, JS has the weakest absolute value of

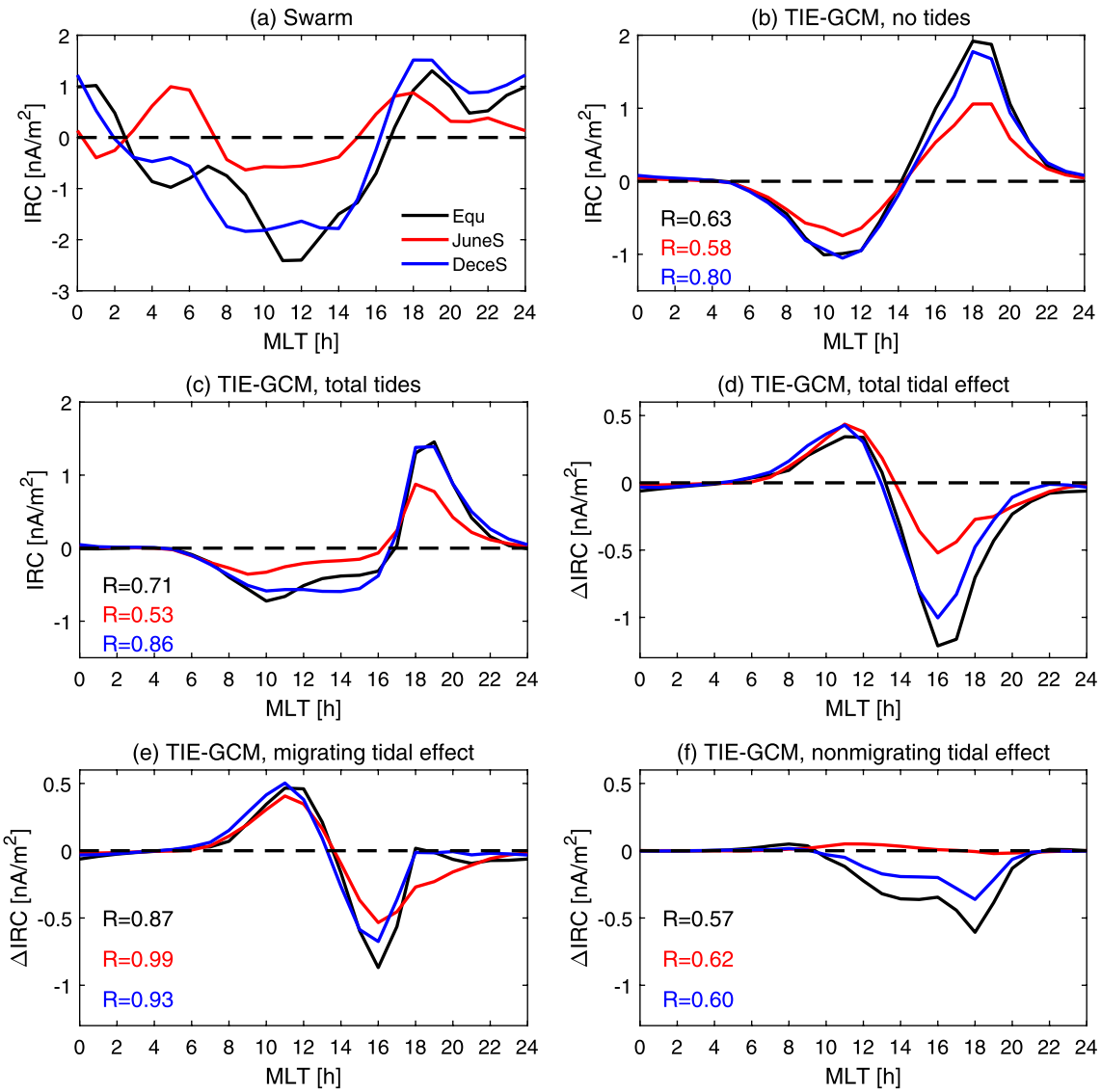

Fig. 2 Diurnal distribution of **a** observed IRC averaged over ± 1° MLat, **b** simulated IRC without tides input, **c** simulated IRC with tides imposed (including migrating and nonmigrating tidal), **d** tidal ΔIRC, **e** migrating tidal ΔIRC, and **f** nonmigrating tidal ΔIRC. Black, red, and blue curves denote the equinox, JS, and DS, respectively. The MLT resolution was 1 h, and positive values represent outward currents. The model IRC are averaged over ± 5° MLat. The linear correlation coefficients in **b** and **c** are calculated relative to the Swarm observations, and the correlation coefficients in **e** and **f** are calculated relative to the total tides effect

inward and outward IRC peaks at noon and dusk. This may be related to the "July minimum" feature of the ionosphere–thermosphere system (Rishbeth and Müller 2007). Interestingly, the reversal local time of IRC from inward to outward direction shows an obvious seasonal dependence: 16–17 MLT in equinox and DS, and 15 MLT in JS, which is consistent with the result of Park et al. (2010).

Figure 2b shows the TIE–GCM simulation without tidal input at the lower boundary of the model, and Fig. 2c shows the simulation results with both migrating and nonmigrating tides imposed. It can be seen that the model performs better over a large range of daytime than in the night-time. This is because that the night-time ionosphere conductivity in TIE–GCM is set close to zero, while it is non-zero in reality. The simulated IRC has inward current around the noontime and outward current on the dusk side, irrespective of the tidal input. This is consistent with the large-scale swarm observations. In the case of tidal input, the consistency

between the daytime variations of simulated IRC and the large-scale observations is better than that in the case of no tidal input, except for the further reduced amplitude. One could notice that under the condition of no tidal input, the swift from the inward to outward current occurs around 14 MLT and from outward to inward around 04 MLT, showing no seasonal difference. However, with the tidal input, the reverse time from outward to inward IRC in the afternoon changes with season. IRC in the JS is about 1 h earlier than that in the equinox, which is more consistent with the observations. This indicates that low atmospheric tide has a significant effect on the seasonal variation of the reverse time in the afternoon.

There are several other parameters that can affect the reverse local time of IRC. Liu et al. (2006) found that the reverse time of thermospheric zonal wind was dependent on solar flux and geomagnetic activity. Because the direction of the thermospheric zonal wind is the main factor determining the IRC direction (Lühr et al. 2019), the reverse time of the IRC should also be affected by solar flux and geomagnetic activity. The Swarm observations are an accumulation of results over 5 years, while the model simulations are a 1-day result with an average solar activity of 100 sfu, hemispheric power of 18 GW, cross polar cap potential of 30 kV. This means that the reverse time of the observed IRC might be influenced by the accumulative results of the solar flux and geomagnetic activity over a 5-year period, while the reverse time of simulated IRC is the result of the simulation under specific conditions of solar flux and geomagnetic activity. The real solar and geomagnetic activity change rapidly with time. In addition, TIE–GCM cannot accurately capture small-scale perturbations, which is the common disadvantage of physical model. These factors may be responsible for the discrepancy of reverse local time between the observed and simulated IRC.

Comparing Fig. 2b, c, it can be found that the lower atmospheric tides have a further weakening effect on the IRC. Taking the equinox as an example, after imposing the lower atmospheric tides, the peak value of inward current at noon decreased from the original -1.01 nA/m^2 to -0.72 nA/m^2 (the negative represents inward), and the peak value of the outward current on the dark side decreased from 1.92 nA/m^2 to 1.46 nA/m^2. There have been no previous reports confirming that tides tend to suppress the intensity of IRC. The underlying reason may be that the zonal wind direction at low altitudes is opposite to that at high altitudes (Wang et al. 2022). Subsequently, the wind speed at F region can be retarded by adding the low atmospheric forcing (i.e., tides). Wang et al. (2021) also found that the lower atmospheric tides tend to suppress the super-rotation of neutral wind in the F region.

One could also notice that the intensity of the dusktime IRC is generally comparable to the observed IRC in the case of tidal input. While the noontime IRC is generally underestimated by 58.2% and 42.8% in equinox and DS without tidal input, and 69.9%, 43.9%, and 67.7% in equinox, JS, and DS with tidal input (see Fig. 2b, c). For example, during the equinox, the peak value of observed IRC at noon is -2.41 nA/m^2, and peak values of simulated IRC without and with tidal effect are -1.01 and -0.72 nA/m^2, respectively. This underestimation of the noontime current density might be due to the fact that the noontime neutral winds are underestimated in the TIE–GCM (e.g., Wang et al. 2021; Zhang et al. 2018). The underestimation of the neutral wind pattern by physical models might be due to the following factors. One possible reason may be related to the model resolution, which may affect the magnitude of outputs. The horizontal resolution of TIE–GCM is 2.5° in geographic latitude (GLat), while it is 0.06° at GLat for Swarm samples. This means that the model can only reproduce large-scale structure, as expected, it is weaker than relatively fine-scale observation. Deng and Ridley (2006) found that when the latitudinal resolution changed from 5° to 1.5° in GITM, the neutral gas heating rate could increase by 20%, because the model could better capture small-scale electric field and particle precipitation. Another factor is that TIE–GCM is based on the empirical high-latitude electric field Heelis model, which only predicts the average state of the high-latitude ion convection for a given 3-hourly Kp index. The real geomagnetic activity changes rapidly with time, potentially causing differences between model predictions and satellite observations. Hence, in the present work we mainly focus on the trend of large-scale longitudinal variation of IRC around the noontime and dusk time using the model in a qualitative way.

To determine which version of TIE–GCM (with or without tidal inputs) fits better with the observations, a correlation analysis has been performed. In Fig. 2b, c, the correlation coefficients between simulations without (with) tides and observations in equinox, JS and Ds are 0.63, 0.58 and 0.80 (0.71, 0.53, and 0.86), respectively. It can be seen that the simulations with tides performs slightly better with observations than those without tides at equinox and DS. The correlation coefficients in JS with and without tides are quite comparable. Thus, the model performs better with the lower atmospheric tides, which supports our conclusion that the atmospheric tides play important roles in the diurnal and seasonal variation of IRC.

Figure 2d shows the total tidal effects on ΔIRC, which is the difference between the case with and without tidal inputs (Fig. 2 b, c). Both the inward IRC around noon and the outward IRC in the afternoon are weakened in all seasons due to the tidal effects. The tidal reduction effect in the dusk is the largest in the equinox and smallest in the JS. The effects of migrating and nonmigrating tides are further separated in TIE–GCM, which are shown in Fig. 2e, f, respectively. Here, the no tidal case is subtracted from the case with migrating or nonmigrating tides. In Fig. 2e, the migrating tides weaken the inward IRC at noon (08–13 MLT), with a peak value at 11 MLT, and weaken the outward IRC at 14–18 MLT with a peak around 16 MLT. At 18–24 MLT, the migrating tidal effect on IRC is negligible in equinox and DS. In Fig. 2f, at 10–22 MLT, IRC due to nonmigrating tides is inward in both equinoxes and DS, reaching a peak value of -0.61 nA/m^2 and -0.36 nA/m^2 at 18 MLT, respectively. The nonmigrating tidal effect on the JS IRC is negligible.

Furthermore, a correlation analysis between simulations with migrating (non-migrating) and total tides is carried out. The migrating (nonmigrating) tidal

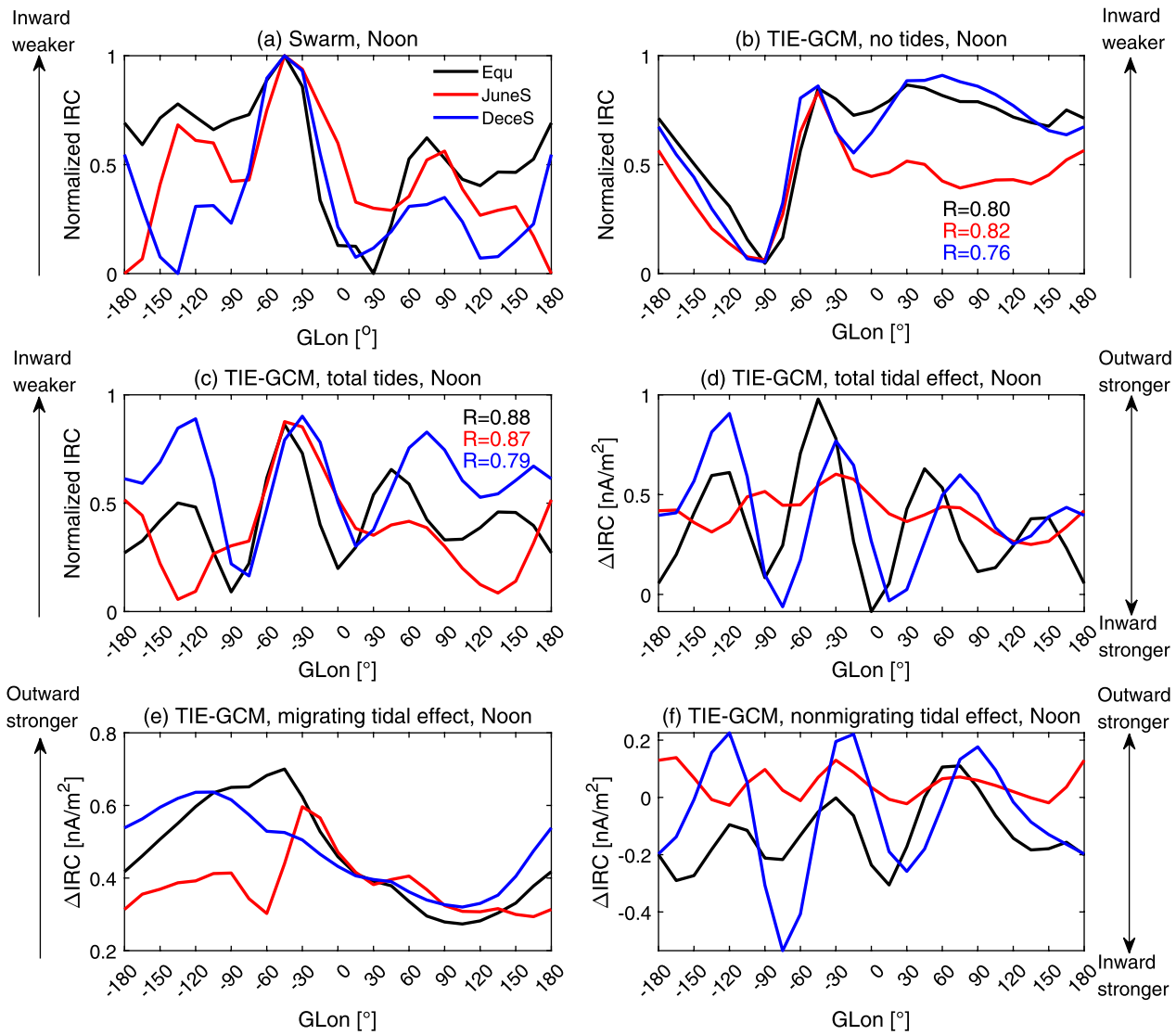

Fig. 3 Longitudinal distribution of the normalized IRC around noon as observed by Swarm satellites (**a**). **b** TIE–GCM-simulated IRC without tidal input. **c** TIE–GCM IRC with total tidal inputs. **d**–**f** Residual IRC induced by **d** total tides, **e** migrating tides, and **f** nonmigrating tides, respectively. Black, red, and blue curves denote the equinox, JS, and DS, respectively. Larger normalized IRC in (**a**–**c**) represent weaker inward currents. Positive values in (**d**–**f**) represent outward currents. The correlation coefficients between model outputs and observations are given for each season. Arrows (double arrows) represent the direction in which the inward or outward current becomes stronger or weaker

effects are highly correlated with the total tidal effects, with a coefficient of 0.87, 0.99 and 0.93 (0.57, 0.62, and 0.60) in equinox, JS, and DS, respectively. The correlation of the effect of migrating and total tides (Fig. 3e, d) is higher than that of the non-migrating tide (Fig. 3f, d), which indicates the dominant role of migrating tide.

Longitudinal variation

The IRC is directed in opposite ways in the noon and dusk sectors. Thus, we investigate the longitudinal IRC variation for these two local times separately. Figure 2a indicates that the MLT when the noontime IRC attains a peak varied in different seasons. Therefore, we adopt the same method as Lühr et al. (2019) for the noon sectors: 10–14 MLT in the JS and 11–15 MLT in other seasons. For the dusk sector: 17–19 MLT in the JS and 18–20 MLT in other seasons. For the TIE–GCM model, we choose 09–11 MLT and 18–20 MLT as the noon and dusk times, respectively, based on the local time of the maximum value in the model results.

Figure 3a, c shows the longitudinal distribution of the modeled and observed IRC in the noontime. The Swarm observations are selected within ± 1° MLat, and the model outputs are selected within ± 5° MLat. The longitude resolution is 15° GLon. Here, we use the normalized IRC, which is defined as $[\mathrm{IRC} - \mathrm{IRC}_{\mathrm{min}}]/[\mathrm{IRC}_{\mathrm{max}} - \mathrm{IRC}_{\mathrm{min}}]$, where $\mathrm{IRC}_{\mathrm{max}}$ and $\mathrm{IRC}_{\mathrm{min}}$ are longitudinal maximum and minimum IRC in each season. In this way the range of the normalized current density is set within 0 and 1, which makes the longitudinal structure more prominent. Note that the IRC directs inward (negative value) in the noontime, thus, the larger positive value denotes weaker inward current, and the smaller value denotes stronger inward current.

In Fig. 3a, the observed IRC has an obvious wave-4 zonal structure. For example, IRC in DS had troughs (peaks) at −135°, −90°, 15°, and 120° GLon (−180°, −120°, −45°, and 90° GLon). The inward IRC was the weakest around −45° GLon in all seasons. The longitudinal averaged current density in the eastern hemisphere (0°–180° GLon) is higher than that in the western hemisphere (−180° to 0° GLon). In Fig. 3b, without tidal input, the longitudinal averaged IRC are stronger in the western hemisphere than that in the eastern hemisphere in all seasons. The observed hemispheric asymmetry is not well-captured by the model without tidal input.

In Fig. 3c, the noontime IRC with tidal input (including migrating and nonmigrating tides) shows an obvious wave-4 structure in equinox and DS, which is quite comparable to the observations. A wave-3 longitudinal structure is shown in JS, which is a little different from the observed wave-4 structure. Note that Swarm observation is the accumulation of results over the years, while model simulation is the result of one single day. The observed IRC is caused by averaging the low-level atmospheric tides on different days, while the simulated IRC is affected by the GSWM empirical atmospheric tides at the equinox and solstice. The actual tides are more complex than the simulation, which may lead to the phase difference between the model and the observation. Thus, to obtain the optimal correlation coefficient, the JS IRC (red curve in Fig. 3c) is shifted by 15° GLon to the east. There is no phase shift in other seasons to obtain the optimal correlation, indicating the better performance of the model in equinox and DS.

Similar to Fig. 2, the correlation analysis between observations and simulations with or without tides are performed to determine which version of TIE–GCM fits better with the observation. The correlation coefficients between observations and simulations without (with) tides are 0.80, 0.82, and 0.76 (0.88, 0.87, and 0.79) in equinox, JS and DS, respectively. It can be found that the simulations with tidal inputs match better with observations than those without tides.

Figure 3d shows the migrating and nonmigrating tidal effects on ΔIRC. Here, ΔIRC represents the difference between the cases with and without tidal inputs. It can be seen that ΔIRC is mostly positive (outward deflection), indicating the weakening effect of tides on the noontime inward current. The zonal wave structure is quite similar to Fig. 3c, although Fig. 3c shows the normalized IRC and Fig. 3d shows the ΔIRC. The effects from migrating and nonmigrating tides are further separated, as shown in Fig. 3e, f. In Fig. 3e, it is clear that ΔIRC induced by migrating tides has a wave 1–2 structure that directs outward. The western hemisphere shows a stronger zonal mean current in the outward direction than the eastern hemisphere, indicating that migrating tides tend to weaken the noontime inward IRC in the western hemisphere more than that in the eastern hemisphere. This indicates that the migrating tides can contribute to the observed trend of east–west difference: larger inward current in the eastern hemisphere than in the western hemisphere (see Fig. 3a). In Fig. 3f, ΔIRC exhibits a wave-4 longitudinal structure in equinox and JS, and exhibits a wave-3 longitudinal structure in DS.

Figure 4a–c shows the longitudinal variations of the normalized IRC in the dusk sector, which is in the same format as in Fig. 3. Note that the more positive value denotes the stronger current in the outward direction. As shown in Fig. 4a, the observed normalized IRC shows larger outward current densities in the western hemisphere than in the eastern hemisphere on a large scale. IRC in the equinox has a large enhancement near −60° to −30° GLon, i.e., in the South Atlantic Anomaly region. This specific feature is not prominent

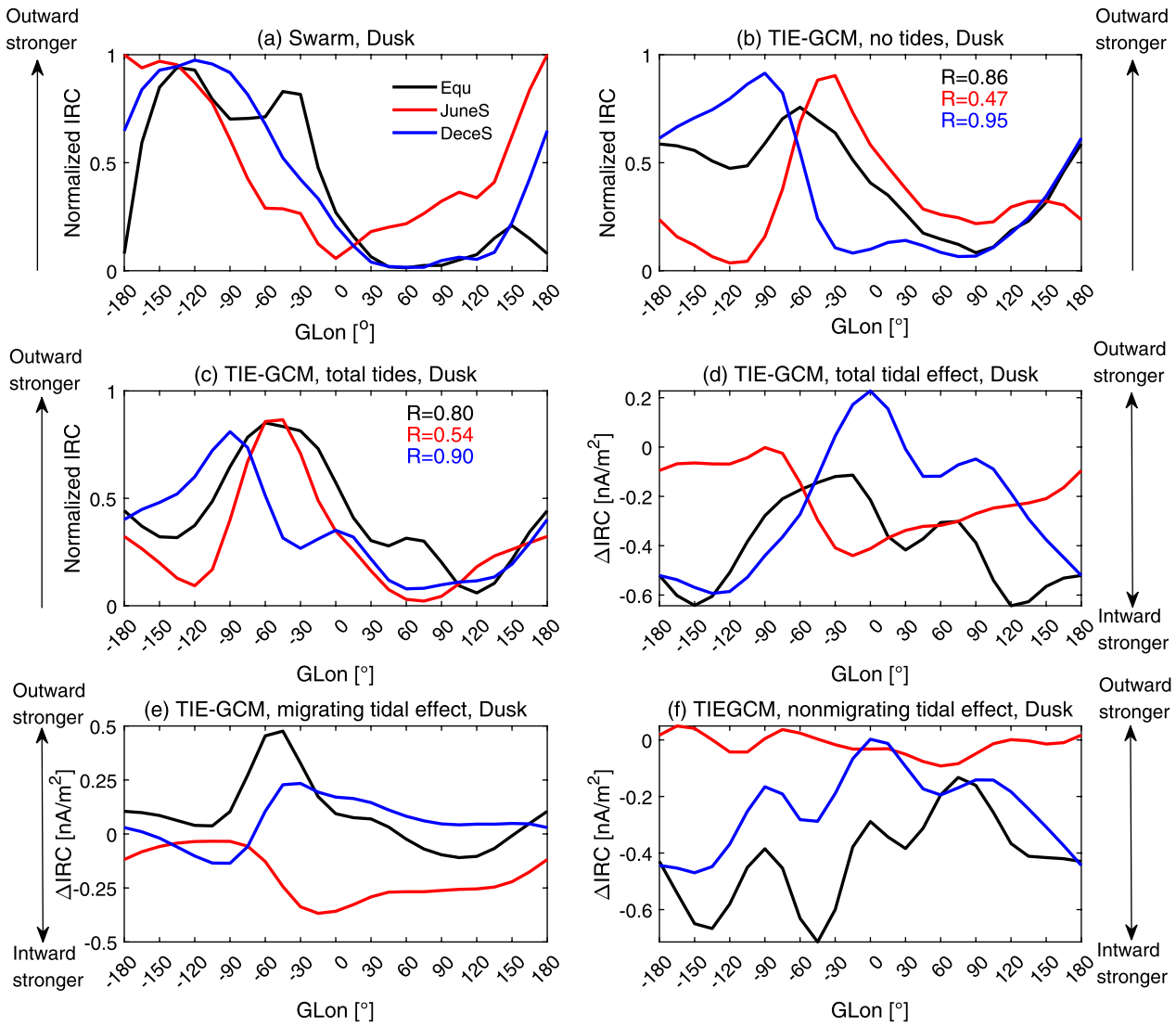

Fig. 4 Similar to Fig. 3, but for dusk IRC. Larger normalized IRC in **a**–**c** represent stronger outward currents. Positive values in **d**–**f** represent outward currents. The correlation coefficients between model outputs and observations are given for each season. Arrows (double arrows) represent the direction in which the inward or outward current becomes stronger or weaker

in the solstices. As shown in Fig. 4b, the normalized IRC simulated by TIE–GCM without tidal input shows a larger current around −45°, −60° and −90° GLon in the JS, equinox and DS. However, when examining the zonal averaged IRC in the model, it is stronger in the western hemisphere (−180° to 0° GLon) than that in the eastern hemisphere (0°–180° GLon). This is generally consistent with the observation. As shown in Fig. 4c, when the low atmospheric tide is applied to the model, the normalized IRC still exhibits a wave-1 structure on a large scale. However, due to the tide, a small amplitude oscillation is superposed. This indicates that the influence of tides on the dusk side is not as significant as that on the dawn side. The low conductivity of the E-layer and the weak coupling of the E–F layer on the duskside might reduce the upward propagation efficiency of tidal waves. Similar to Fig. 3, the correlation analyses are performed between the observation (Fig. 4a) and model without tides (Fig. 4b) and with tides (Fig. 4c). The correlation coefficients between simulations without (with) tides and observations in equinox, JS and Ds are 0.86, 0.47, and 0.95 (0.80, 0.54, and 0.90), respectively. The correlation in JS improves with tidal input, but decreases slightly in other seasons.

Figure 4d shows the tidal effects on the longitudinal distribution of the duskside ΔIRC (difference between

the case with tides and the case without tides). In all seasons, ΔIRC caused by lower atmosphere tides is almost inward (negative value denotes inward direction), which indicates that the IRC is weakened by tides. Furthermore, ΔIRC shows wave 1, 2–3 structure in JS, DS and equinox. In Fig. 4e, in equinox (DS), ΔIRC caused by the migrating tides has a peak upward enhancement at −45° (−30°) GLon, while in the remaining longitudes, the migrating tide has a less enhancement even reduced on the upward IRC. In JS, the weakening effects of migrating tides on the outward IRC are weaker in the western hemisphere than that in the eastern hemisphere. This indicates that the migrating tides contribute to the east–west hemispheric asymmetry of IRC. Figure 4f shows the effect of nonmigrating tides on the duskside IRC. The nonmigrating tides cause wave 3–4 structures in DS and equinox. There is a weak ΔIRC fluctuating around zero in JS, which will be discussed in "Effects of tides on longitudinal IRC distribution".

Discussion

Effects of tides on diurnal IRC distribution

Using observations of the Swarm satellites, Lühr et al. (2019) found that in the noontime the absolute value of the inward IRC density is the minimum in the JS and maximum in the equinox. Our observations and simulations are consistent with this seasonal variation. This is consistent with the so called "July minimum" feature of the ionosphere–thermosphere system (Rishbeth and Müller 2007). Lühr et al. (2019) revealed that the noontime IRC is larger than that in the dusk sector in the equinox and DS. As shown in Fig. 2d, the migrating and nonmigrating tides together reduce inward IRC at noontime and decrease the outward IRC in the dusk sector, with weaker reduction at noon than at dusk-time (Fig. 2d). This indicates that lower atmospheric tides might partly account for the noon-dusk difference in IRC.

The discrepancy between model simulations and Swarm observations might be related to the following four reasons. First, the Swarm observations are an accumulation of results over 5 years, while the model simulations are a 1-day result with an average solar activity of 100 sfu, hemispheric power of 18 GW, cross polar cap potential of 30 kV. The complex structures of IRC observations are possibly induced by averaging over different days with varying lower atmospheric waves and geomagnetic and solar activity forcing. The real geomagnetic conditions are complicated, causing the differences between model outputs and Swarm observations. Second, the lower atmospheric tides from GSWM are imposed into the lower boundary of TIE–GCM. The GSWM-generated tides are empirical, potential causing the model-observation discrepancy. Third, previous studies have disclosed that the quiet-time thermospheric winds in F-region have been underestimated in the physical models, including TIE–GCM (e.g.,Wang et al. 2021; Zhang et al. 2018). IRC has been deeply influenced by the thermospheric winds, hence causing the model-observation discrepancy. Fourth, it may be related to the empirical specification of the auroral inputs in the TIE–GCM, which is described in detail in Roble and Ridley (1987). Because auroral precipitation and convection patterns in the TIE–GCM are specified by empirical models, Joule heating and ion drag caused by high-latitude inputs might be different from the real case. In addition, the energy input at high latitude is held constant in the simulation, while it is varying in reality. Although the model cannot accurately reproduce the amplitude of the observed current and the reverse local time, the results show that the simulated IRC with tidal input correctly reproduce the large-scale inward current around noon and outward current at dusk, and there is a good correlation between the observed and simulated IRC in terms of longitudinal change trend. This shows that the model results are still of reference significance. In the current work, we mainly focus on the trend change of IRC in a qualitative way using the model.

The F region IRC can be derived using the equation:$j_z = \sigma_P(u_y B_x - E_z)$ (Park and Lühr, 2012). The first term on the right side of the equation, $\sigma_P u_y B_x$, is the dynamo current driven by the F region zonal wind. The second term, $-\sigma_P E_z$, represents the current generated by the polarized electric field. Park and Lühr (2013) studied the relative contributions of these two components to the vertical current in the F region. They found that the current driven by the radial electric field is opposite to the wind dynamo current, whereas the vertical current of the F layer is mainly contributed by the wind dynamo. In the daytime, the inward vertical current driven by the westward wind peaks around noon, and the outward vertical current driven by the eastward wind peaks at dusk. Therefore, it is necessary to clarify the relative roles of these two components in the tidal IRC and establish whether dynamo current or the polarization current dominates ΔIRC?.

We calculate two components, $-\sigma_P E_z$ and $\sigma_P u_y B_x$, for the case without tidal input, and the results are shown in Fig. 5a, b. The directions of both current components are opposite to each other: $-\sigma_P E_z$ is outward at noon and inward at dusk, whereas $\sigma_P u_y B_x$ is inward at noon and outward at dusk. The dynamo current is larger in amplitude than the polarization current around noon and dusk. Therefore, the IRC is mainly controlled by the dynamo current, which is consistent with the conclusions of Park and Lühr (2013).

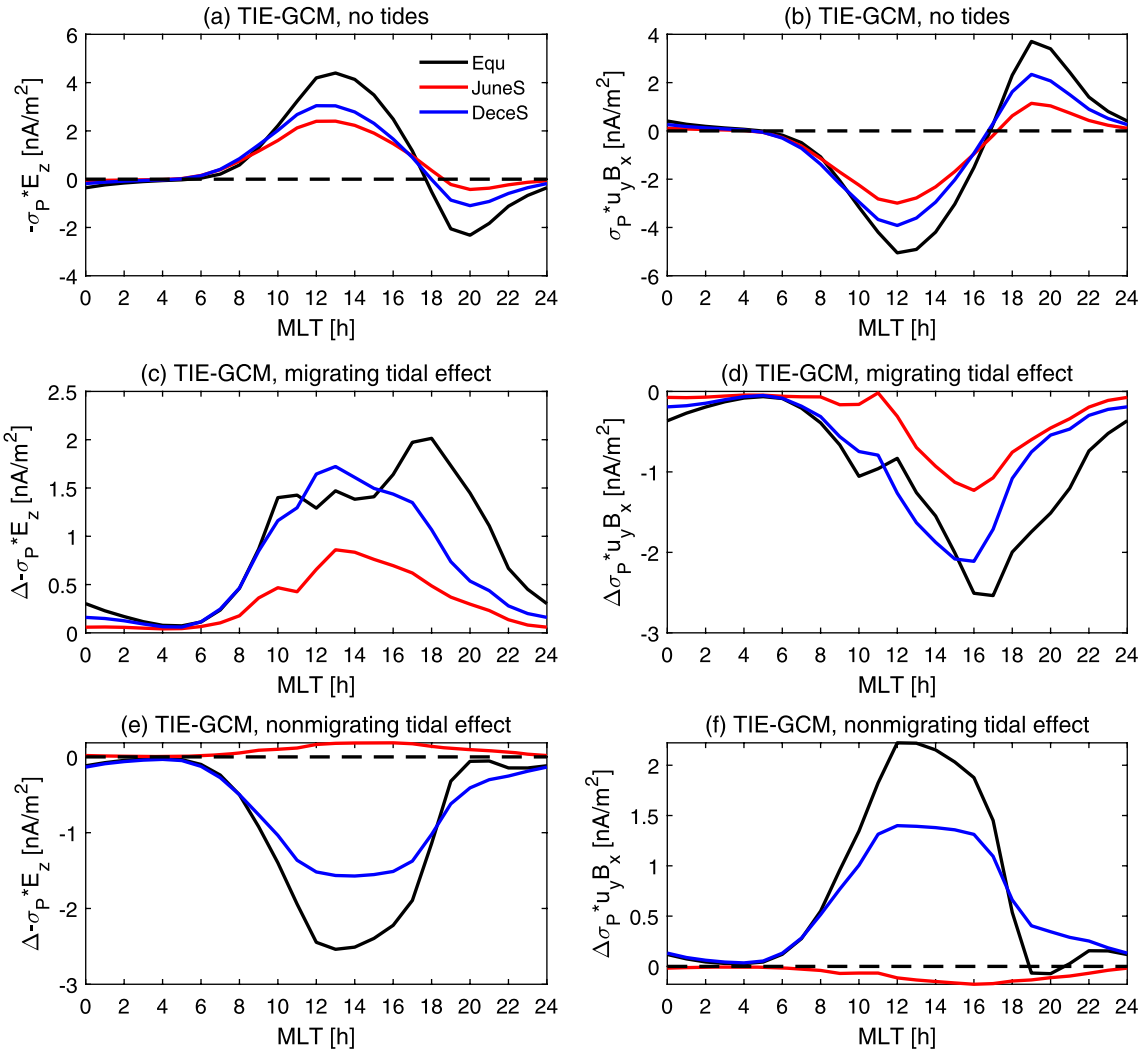

Fig. 5 Local time distribution of the polarization current (left) and dynamo current (right). **a**, **b** IRC without tides; **c**, **d** migrating tidal effect; **e**, **f** nonmigrating tidal effect. Black, red, and blue curves denote the equinox, JS, and DS, respectively. Positive values represent outward currents

The results are different during tidal periods. The migrating tidal effects on the polarization and dynamo currents are shown in Fig. 5c, d. Around the noontime (09–11 MLT), migrating tides enhance both the outward polarization current and inward dynamo current. The enhancement of the polarization current is larger in absolute amplitude than that of dynamo current at noon, and vice versa at dusk. A comparison between Figs. 2e and 5c–d shows that the migrating tides modulate the IRC mainly though the polarization current in the noontime and though the dynamo current around 14–18 MLT.

The effects of nonmigrating tides on these two current components are shown in Fig. 5e, f. The nonmigrating tidal effect is relatively weak in the JS. In the equinox and DS, the dynamo current is mainly directed outward, whereas the polarization current is mostly directed inward, which is opposite to that from the migrating tides. In comparison with Fig. 2f, it can be seen that the nonmigrating tides modulate the IRC mainly though the polarization current. Therefore, the following conclusions can be drawn: the polarization current generated by the migration tide plays a leading role at noon, while the dynamo current due to the migrating tide plays a controlling role at dusk. The ΔIRC is controlled mainly by the polarization current generated by nonmigrating tides in the equinox and DS.

Furthermore, we quantitatively determine the effects of migrating and nonmigrating tides by calculating the relative changes in the noontime (10–12 MLT) and

dusk-time (18–20 MLT) IRCs by calculating the ΔIRC/IRC ratio, where "ΔIRC" is the change in the IRC due to tides and "IRC" is the value obtained during the notide period. A negative change indicated a decreasing effect. For the noontime IRC, the relative changes due to migrating tides (nonmigrating tides) are approximately −47%, −56%, and −49% (13%, −7%, and 7%) in the equinox, JS, and DS, respectively. It is clear that the migrating tidal effect played a dominant role at noontime. For the dusk-time IRC, the relative changes due to migrating tides (nonmigrating tides) are approximately 5%, −22%, and 4% (−26%, −2%, and −17%) in the equinox, JS, and DS, respectively. Therefore, in the dusk side, the ΔIRC of the equinox and DS is mainly controlled by nonmigrating tides, and the ΔIRC of JS is mainly controlled by migrating tides.

Effects of tides on longitudinal IRC distribution

Previous studies have shown a typical wave-4 longitudinal structure closely related to low atmospheric tides in the coupled ionosphere–thermosphere system. For example, the dayside total electron content in the ionosphere has an obvious wave-4 longitudinal structure (Lin et al. 2007). The vertical plasma drift in the F layer shows a wave-4 structure in longitude (Hartman and Heelis 2007). This wave-4 structure is generally associated with an eastward-propagating nonmigrating diurnal tidal mode with wave-3 (DE3) (Park et al. 2010; Oberheide et al. 2011).

The F-region dynamo current is closely related to the neutral zonal wind in the thermosphere. Lühr et al. (2007) predicted that the F-region dynamo current have a wave-4 longitudinal structure. Park et al. (2010) used CHAMP data to reveal the wave-4 structure of the IRC at the magnetic equator and found that the noon-time wave-4 structure is more pronounced due to the DE3 nonmigrating component.

The good correlation between the waves in Fig. 3a, c (Fig. 4a, c) suggests a good correspondence between Swarm observations and TIE–GCM simulations. As shown in Fig. 3e, the migrating tides cause a stronger outward IRC in the western hemisphere than in the eastern hemisphere. This indicates that the previously reported west–east hemispheric asymmetry of the noontime IRC by Lühr et al. (2019) might be caused partly by migrating tides in the low atmosphere. In addition, the nonmigrating tides mainly cause the wave-3 structure of IRC (see Fig. 3f). Oberheide et al. (2011) found that the nonlinear interactions between migrating tides and DE3 drive wave-4 longitudinally structured zonal wind in the equatorial E layer. This suggested that the wave-4 structure of IRC is caused by the combined effects of migrating and nonmigrating tides. In daytime, the F layer inward current is closed by the high-conductivity E layer (Maute and Richmond 2017); therefore, the E region dynamo can be reflected in the F region.

In contrast, there is no prominent wave-4 longitudinal structure in the modeled or observed IRC in the dusk sector. One of the reasons for this is the low conductivity of the night-time E layer, which leads to the weakening of the E–F coupling (Park et al. 2010; Maute and Richmond 2017). The wave-3 or wave-2 longitudinal structures exist due to tides, as shown in Fig. 4d. However, the tidal effect is not evident because of the stronger IRC in the background. Taking the DS as example, the IRC in dusk sector (18–20 MLT) without tidal input is approximately 1.35 nA/m^2 (Fig. 2b), whereas the peak-trough differences in the wave-3 structure of nonmigrating tidal effect are only 0.12, 0.20, and 0.30 nA/m^2 (Fig. 4f). The tidal effect only accounts for 9–22% of the background IRC. In comparison, in DS, the IRC in noontime (10–12 MLT) without tidal input is approximately −0.93 nA/m^2 (Fig. 2b), whereas the peak-trough differences in the wave-3 structure of nonmigrating tidal effect are 0.76, 0.48, and 0.37 nA/m^2 (Fig. 3f). The tidal effect accounts for 40–82% of the background IRC.

There are significant seasonal differences in the influence of atmospheric tides on the longitudinal distribution of IRC. The seasonal variation in IRC may be dominated by changes in atmospheric tides (Park et al. 2020). Lühr and Manoj (2013) summarized the roles of different tidal patterns in the equatorial electrojet for each month. They found that DE3, which caused the wave-4 structure, was the strongest from August to September, and the second-largest nonmigrating component, semi-diurnal SW4, which caused the wave-2 structure, was the strongest in the DS and weakest in the JS. The competitive effects of different nonmigrating components may produce the results in the model: the effect of nonmigrating tides on IRC is stronger in the equinox and DS, and weaker in the JS. The longitudinal wave structure of the simulated IRC in JS is negligible when compared to the observations (Fig. 4f). This may be because the observations were from May to August, when the influence of the nonmigrating tides gradually intensify. However, IRC is simulated in the June solstice, when the influence of nonmigrating tides is weak.

Effect of geomagnetic field configuration

In "Longitudinal variation", we found that observed IRC has east–west hemispheric difference, which is consistent with Lühr et al. (2019). Lühr et al. (2019) revealed that

the IRC intensity showed east–west hemispheric difference in both noontime and dusk-time. This hemispheric difference was found to exist in all seasons. They speculated that this might be related to the geomagnetic field configuration, which is irrespective of season. Moreover, the geomagnetic field strength near the equator varies considerably with longitude, which could influence the longitudinal distributions of ionospheric conductivity, which is an important contributor to the vertical current intensity. Because the geomagnetic configuration plays an important role in the ionosphere–thermosphere coupling system (Doumbia et al. 2007; Zeng et al. 2008; Cnossen and Richmond 2012; Wang and Lühr 2016; Dang et al. 2016; Zhang et al. 2018). Cnossen and Richmond (2012) found that the dipole tilt angle controlled the geographic longitudinal distribution of the Joule heating, furtherly changing the thermospheric temperature and neutral winds. Zhang et al. (2018) also found that the geomagnetic field configuration might dominate the hemispheric asymmetry in the longitudinal structures of zonal winds.

To explore the influences of geomagnetic field on the longitudinal distributions of IRC, we replace the IGRF model with a centered dipole field in the TIE–GCM model.

Figure 6a shows the longitudinal distribution of the northward magnetic field in the frame of the dipole field and IGRF. The IGRF real magnetic field shows one minimum and one maximum at −60° GLon and 105° GLon, whereas there is no longitudinal difference in the dipole magnetic field. Figure 6b shows the local time variation of IRC in the two field configurations. The diurnal variations of IRC in the IGRF and dipole frame are quite comparable, with the strongest outward current in 10–12 MLT and the strongest inward current in 17–19 MLT.

Figure 6c, d shows the longitudinal variation of IRC in the noon and dusk under two geomagnetic field configurations. The simulated IRC in the case of IGRF shows obvious east–west hemispheric differences. When utilizing the dipole model, the simulated IRC shows no longitudinal difference. This confirms that the geomagnetic configuration can account for the east–west hemispheric

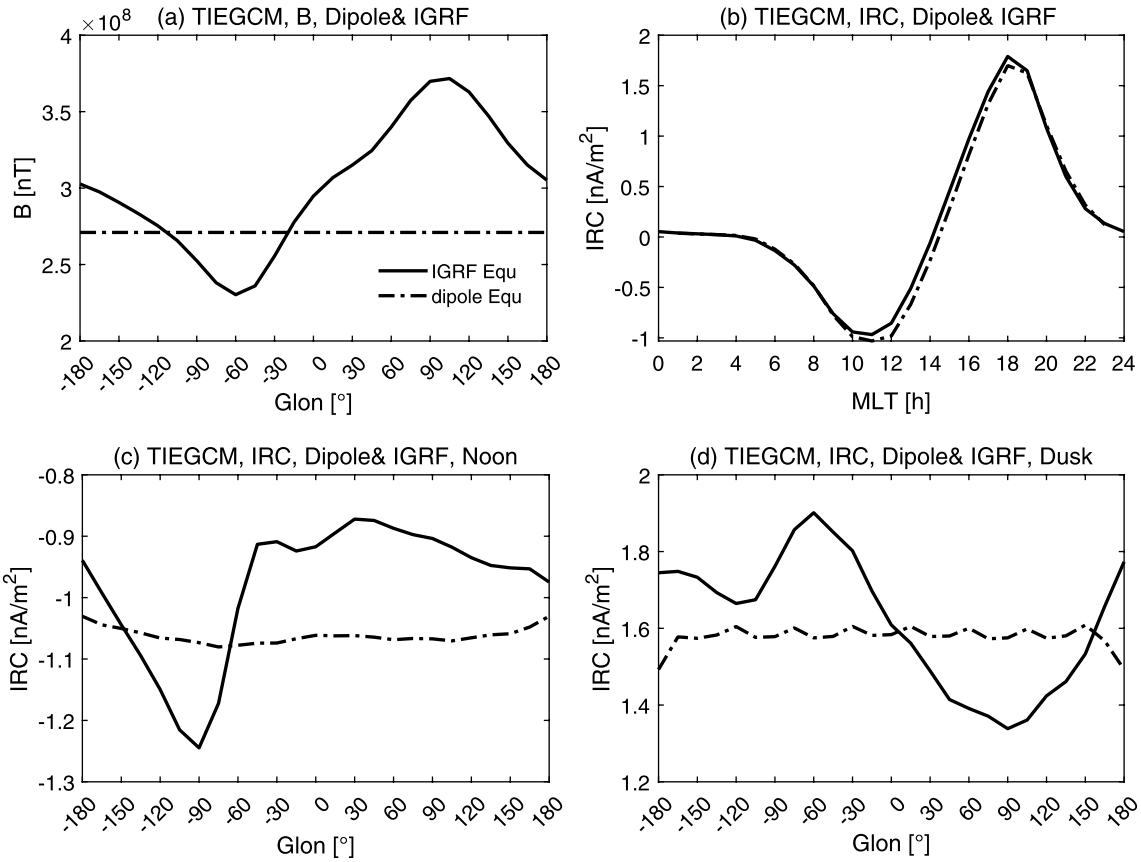

Fig. 6 Longitudinal variations of **a** northward component of magnetic field and **c**, **d** IRC in equinox under two different geomagnetic field configurations: IGRF and dipole cases. **b** MLT variations of IRC in IGRF and dipole cases in equinox. IRC is the longitudinal averaged value. Positive values in **a** represent the northward magnetic field. The solid and dotted lines represent IGRF and dipole results

difference in the IRC. This can be explained by the fact that when the geomagnetic axis coincides with the geographic axis, both the neutral wind and ionospheric conductivity show a homogenous longitudinal distribution; hence, the longitudinal variation of IRC can be negligible.

Hemispheric asymmetry of IRC

A comparison of the results illustrated in Fig. 4a, c demonstrates that the noontime IRC on a large scale, as observed by Swarm satellites, shows a stronger inward current in the eastern hemisphere, whereas IRC simulated by the TIE–GCM shows a larger inward current in the western hemisphere. The observed hemispheric difference might be partly caused by the difference between the satellite orbital and IRC altitude in the western and eastern hemispheres. As explained by Lühr et al. (2019), the noontime dynamo current may be located at a higher altitude in the eastern hemisphere than in the western hemisphere. Thus, Swarm satellites were much closer to the center of IRC in the eastern hemisphere than in the western hemisphere. Unfortunately, the model did not reproduce the longitudinal variation in central IRC height. Therefore, this viewpoint could not be verified in the present study. As outlined in "Effects of tides on longitudinal IRC distribution", the migrating tides cause a stronger outward IRC in the western hemisphere than in the eastern hemisphere, as shown in Fig. 3e. This indicates that the observed west–east hemispheric asymmetry of the noontime IRC might be caused partly by migrating tides in the low atmosphere. If the effect of migration tide is intensified, the model might be capable to reproduce the observed west–east hemispheric differences.

The Swarm observations and TIE–GCM simulations show that the dusk IRC has a stronger outward current in the western hemisphere and a weaker outward current in the eastern hemisphere, which is consistent with previous observations (Park et al. 2010; Lühr et al. 2015, 2019). To identify possible reasons for the longitudinal differences, we compare the dynamo current $\sigma_P u_y B_x$ and polarization current $-\sigma_P E_z$ with the observed values in more detail (Fig. 7). Figure 7a shows the longitudinal distribution of the dynamo current, which peaks in the western hemisphere due to higher conductivity. Figure 7b shows the longitudinal variation of the polarization current, which is opposite to that of the dynamo current and has a weaker current density in absolute value. This indicates that the hemispheric asymmetry of the dusk IRC mainly comes from the neutral wind dynamo effect, with the competing role of the polarization current that finally determines the peak location of the total current in the western hemisphere.

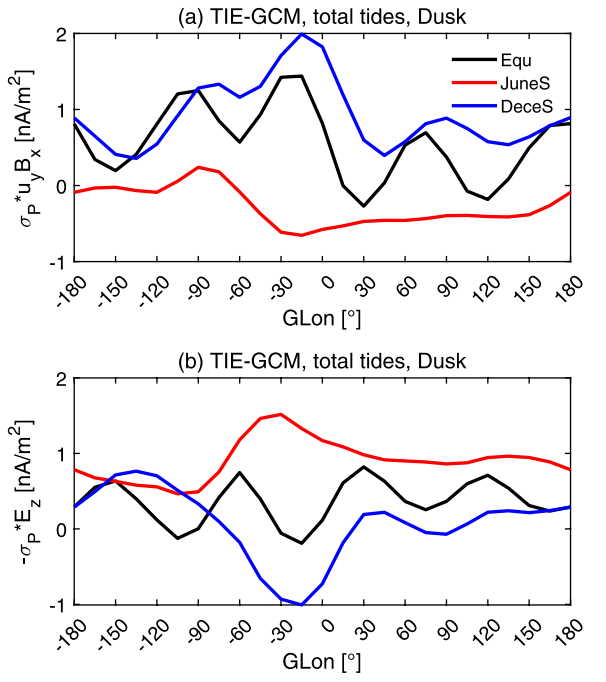

Fig. 7 Longitudinal distributions of the dynamo and polarization currents at dusk sector in equinoxes, JS, and DS. Black, red, and blue curves denote the equinox, JS, and DS. Positive values represent outward currents

Conclusions

Using observations from Swarm dual satellites A and C from 2014 to 2018, we studied the local time and longitudinal variation of IRC in different seasons. Having contrasted actual observations with the results of the TIE–GCM simulations, we discussed the physical mechanisms of IRC variations. Some interesting findings can be summarized as follows:

1. The reverse time from the inward to outward currents occurred earlier in the JS than in other seasons. Low-altitude tides had an important effect on the seasonal change in the reverse time.

2. Both observed and simulated IRC had an obvious wave-4 zonal structure at noontime, which was related to both migrating and nonmigrating tides. The negligible longitudinal variation in the dusk IRC may be related to the weakening of the E–F coupling.

3. Lower atmospheric tides tended to weaken IRC, mainly through their effect on the polarization current at noon, whereas polarization and dynamo current at dusk. The migrating tides played a major weakening role at noon, whereas the nonmigrating tides were more dominant in the equinox and DS at dusk.

4. The geomagnetic configuration was the main reason for the longitudinal variation in IRC. The simulated IRC showed longitudinal variation different from that actually

observed at noontime. This was partly caused by the underestimation of migrating tides.

5. The simulated and observed IRC at dusk are larger in the western hemisphere than in the eastern hemisphere, which could be mainly explained by the wind dynamo current. The competitive effect of the dynamo and polarization currents determined the peak position of the total current in the western hemisphere.

Abbreviations

TIE–GCM: Thermosphere–ionosphere electrodynamic–general circulation model; GSWM: Global scale wave model; IRC: Ionospheric radial current; JS: June solstice; DS: December solstice; MLT: Magnetic local time; LT: Local time; GLon: Geographic longitude; GLat: Geographic latitude; MLat: Magnetic latitude.

Acknowledgements

The authors greatly appreciate the availability of data. We are grateful to the Editor and anonymous reviewers for their assistance in improving the manuscript. The European Space Agency (ESA) is acknowledged for providing the Swarm data and for financially supporting the work of developing the Level-2, CAT-2 products. The IRC data used here are the Swarm Level-2 product FAC (FAC_TMS_2F) that is freely accessible to all users via ftp://swarm-diss.eo.esa.int/Level2daily/Latest_baselines/ FAC/TMS/Sat_AC/.

Author contributions

Conceptualization, HX and HW; methodology, HX; software, KZ; validation, HX; formal analysis, YZ; investigation, CQ; resources, HW; data curation, HX; writing—original draft preparation, HX; writing—review and editing, HW; visualization, HX; supervision, HW; project administration, HW; funding acquisition, HW. All author read and approved the final manuscript.

Funding

This research was funded by the National Natural Science Foundation of China Basic Science Center (42188101), the Fundamental Research Funds for the Central Universities (2042021kf0208), National Nature Science Foundation of China (41974182), and Hubei Province Outstanding Youth Project (2017CFA057).

Availability of data and materials

The Level-2 radial current data product is available at the European Space Agency FTP site ftp://swarm-diss.eo.esa.int under the directory of/Level2daily/Latest_baselines/FAC/TMS/. The solar wind and interplanetary magnetic field and magnetic activity index data are from NASA/GSFC'S Space Physics Data Facility's OMNIWeb (https://omniweb.gsfc.nasa.gov).

Declarations

Competing interests

The authors declare that they have no competing interests.

Received: 13 May 2022 Accepted: 30 September 2022
Published online: 12 October 2022

References

Cnossen I, Richmond AD (2012) How changes in the tilt angle of the geomagnetic dipole affect the coupled magnetosphere-ionosphere-thermosphere system. J Geophys Res 117:A10317. https://doi.org/10.1029/2012JA018056

Dang T, Luan X, Lei J, Dou X, Wan W (2016) A numerical study of the interhemispheric asymmetry of the equatorial ionization anomaly in solstice at solar minimum. J Geophys Res Space Physics 121:9099–9110. https://doi.org/10.1002/2016JA023012

Deng Y, Ridley AJ (2006) Dependence of neutral winds on convection E-field, solar EUV, and auroral particle precipitation at high latitudes. J Geophys Res 111:A09306. https://doi.org/10.1029/2005JA01

Doumbia V, Maute A, Richmond AD (2007) Simulation of equatorial electrojet magnetic effects with the thermosphere-ionosphere-electrodynamics general circulation model. J Geophys Res 112:A09309. https://doi.org/10.1029/2007JA012308

Finlay CC, Olsen N, Kotsiaros S, Gillet N, Tøffner-Clausen L (2016) Recent geomagnetic secular variation from Swarm and ground observatories as estimated in the CHAOS-6 geomagnetic field model. Planets Space 68:112. https://doi.org/10.1186/s40623-016-0486-1

Fukushima N (1979) Electric potential difference between conjugate points in middle latitudes caused by asymmetric dynamo in the ionosphere. J Geomagn Geoelectr 31:401–409. https://doi.org/10.5636/jgg.31.401

Hagan ME, Forbes JM (2002) Migrating and nonmigrating diurnal tides in the middle and upper atmosphere excited by tropospheric latent heat release. J Geophys Res 107(D24):4754. https://doi.org/10.1029/2001JD001236

Hartman WA, Heelis RA (2007) Longitudinal variations in the equatorial vertical drift in the topside ionosphere. J Geophys Res 112:A03305. https://doi.org/10.1029/2006JA011773

Heelis RA, Lowell JK, Spiro RW (1982) A model of the high-latitude ionospheric convection pattern. J Geophys Res 87(A8):6339–6345. https://doi.org/10.1029/JA087iA08p06339

Lin CH, Hsiao CC, Liu JY, Liu CH (2007) Longitudinal structure of the equatorial ionosphere: Time evolution of the four-peaked EIA structure. J Geophys Res 112:A12305. https://doi.org/10.1029/2007JA012455

Liu H, Lühr H, Watanabe S, Köhler W, Henize V, Visser P (2006) Zonal winds in the equatorial upper thermosphere: decomposing the solar flux, geomagnetic activity, and seasonal dependencies. J Geophys Res 111:A07307. https://doi.org/10.1029/2005JA011415

Lühr H, Manoj C (2013) The complete spectrum of the equatorial electrojet related to solar tides: CHAMP observations. Ann Geophys 31:1315–1331. https://doi.org/10.5194/angeo-31-1315-2013

Lühr H, Maus S (2006) Direct observation of the F region dynamo currents and the spatial structure of the EEJ by CHAMP. Geophys Res Lett 33:L24102. https://doi.org/10.1029/2006GL028374

Lühr H, Häusler K, Stolle C (2007) Longitudinal variation of F region electron density and thermospheric zonal wind caused by atmospheric tides. Geophys Res Lett 34:L16102. https://doi.org/10.1029/2007GL030639

Lühr H, Kervalishvili GN, Michaelis I, Rauberg J, Ritter P, Park J, Merayo JMG, Brauer P (2015) The interhemispheric and F region dynamo currents revisited with the Swarm constellation. Geophys Res Lett 42:3069–3075. https://doi.org/10.1002/2015GL063662

Lühr H, Kervalishvili GN, Stolle C, Rauberg J, Michaelis I (2019) Average characteristics of low-latitude interhemispheric and F region dynamo currents deduced from the swarm satellite constellation. J Geophys Res Space Phys 124:10631–10644. https://doi.org/10.1029/2019JA027419

Lühr H, Ritter P, Kervalishvili G, Rauberg J (2020) Applying the dual-spacecraft approach to the swarm constellation for deriving radial current density. In: Dunlop MW, Lühr H (eds) Ionospheric multi-spacecraft analysis tools, ISSI scientific report series 17. Switzerland, Springer Nature, pp 117–140

Maeda H, Iyemori T, Araki T, Kamei T (1982) New evidence of a meridional current system in the equatorial ionosphere. Geophys Res Lett 9:337–340. https://doi.org/10.1029/GL009i004p00337

Maute A, Richmond AD (2017) F-region dynamo simulations at low and mid-latitude. Space Sci Rev 206:471–493. https://doi.org/10.1007/s11214-016-0262-3

Oberheide J, Forbes JM, Zhang X, Bruinsma SL (2011) Wave-driven variability in the ionosphere-thermosphere-mesosphere system from TIMED observations: What contributes to the "wave 4"? J Geophys Res 116:A01306. https://doi.org/10.1029/2010JA015911

Olsen N (1997) Ionospheric F region currents at middle and low latitudes estimated from Magsat data. J Geophys Res 102(A3):4563–4576. https://doi.org/10.1029/96JA02949

Park J, Lühr H (2012) Effects of sudden stratospheric warming (SSW) on the lunitidal modulation of the F-region dynamo. J Geophys Res 117:A09320. https://doi.org/10.1029/2012JA018035

Park J, Lühr H (2013) Relation of zonal plasma drift and wind in the equatorial F region as derived from CHAMP observations. Ann Geophys 31:1035–1044. https://doi.org/10.5194/angeo-31-1035-2013

Park J, Lühr H, Min KW (2010) Characteristics of F-region dynamo currents deduced from CHAMP magnetic field measurements. J Geophys Res 115:A10302. https://doi.org/10.1029/2010JA016265
Park J, Lühr H, Min KW (2011) Climatology of the inter-hemispheric field-aligned current system in the equatorial ionosphere as observed by CHAMP. Ann Geophys 29:573–582. https://doi.org/10.5194/angeo-29-573-2011
Park J, Yamazaki Y, Lühr H (2020) Latitude dependence of interhemispheric field-aligned currents (IHFACs) as observed by the swarm constellation. J G R Space Phys. https://doi.org/10.1029/2019JA027694
Richards PG, Fennelly JA, Torr DG (1994) EUVAC: a solar EUV flux model for aeronomic calculations. J Geophys Res 99(A5):8981–8992. https://doi.org/10.1029/94JA00518
Richmond AD (1995) Ionospheric electrodynamics using magnetic apex coordinates. J Geomagn Geoelectr 47:191. https://doi.org/10.5636/jgg.47.191
Rishbeth H (1971a) The F- layer dynamo. Planet Space Sci 19(2):263–267. https://doi.org/10.1016/0032-0633(71)90205-4
Rishbeth H (1971b) Polarization fields produced by winds in the equatorial F-region. Planet Space Sci 19:357–369. https://doi.org/10.1016/0032-0633(71)90098-5
Rishbeth H, Müller-Wodarg ICF (2007) Why is there more ionosphere in January than in July? The annual asymmetry in the F2-layer. Ann Geophys 24:3293–3311. https://doi.org/10.5194/angeo-24-3293-2006
Ritter P, Lühr H, Rauberg J (2013) Determining field-aligned currents with the Swarm constellation mission. Earth Planet Sp 65:9. https://doi.org/10.5047/eps.2013.09.006
Roble RG, Ridley EC (1987) An auroral model for the NCAR thermospheric general circulation model (tgcm). Ann Geophys 5(6):369–382
Wang H, Lühr H, Zhang KD (2021) Longitudinal variation in the thermospheric superrotation: CHAMP observation and TIE-GCM simulation. Geophys Res Lett. https://doi.org/10.1029/2021GL095439
Wang H, Gao J, Zhang K (2022) Influence of the magnetic field strength and solar activity on the thermospheric zonal wind. JGR Space Phys. https://doi.org/10.1029/2021JA029741
Wang H, Luhr H (2016) Longitudinal variation in zonal winds at subauroral regions: possible mechanisms. J Geophys Res Space Phys 121:745–763. https://doi.org/10.1002/2015JA022086
Zeng Z, Burns A, Wang W, Lei J, Solomon S, Syndergaard S et al (2008) Ionospheric annual asymmetry observed by the COSMIC radio occultation measurements and simulated by the TIEGCM. J Geophys Res 113:A03308. https://doi.org/10.1029/2007JA012897
Zhang K, Wang W, Wang H, Dang T, Liu J, Wu Q (2018) The longitudinal variations of upper thermospheric zonal winds observed by the CHAMP satellite at low and midlatitudes. J G R Space Physics. https://doi.org/10.1029/2018JA025463

Publisher's Note